On the emitter formation in nanotextured silicon solar cells to achieve improved electrical performances

Bishal Kafle [a,*], Jonas Schön [a], Christoph Fleischmann [a], Sabrina Werner [a], Andreas Wolf [a], Laurent Clochard [b], Edward Duffy [b], Marc Hofmann [a], Jochen Rentsch [a]

[a] Fraunhofer Institute for Solar Energy Systems (ISE), Heidenhofstr. 2, 79110 Freiburg, Germany
[b] Nines Photovoltaics, Synergy Centre, IT Tallaght, Dublin 24, Ireland

ABSTRACT

In this paper, we study the effect of an enlarged surface area of nanotextured crystalline silicon wafers on the formation of n-type emitters using a tube diffusion process applying $POCl_3$ as P dopant source. A fast, single-step and industrially viable F_2-based dry texturing process is used to perform nanotexturing of Si wafers. This process is presented as an alternative route of nanotexturing in comparison to the two-step nanotexturing approach of creating black silicon and then modifying it with an alkaline or acidic solution. Predictive simulations of phosphorous in-diffusion aided by microscopical characterization of the selected emitters are used to understand the formation of emitter in nanotextured surfaces. Based on these investigations, we show that the optimized emitter leads to a significant improvement in short circuit current density ($J_{sc} \geq 0.7$ mA/cm²) of nanotextured mc-Si solar cells in comparison to the industrial standard acidic textured solar cells.

© 2016 Elsevier B.V. All rights reserved.

1. Introduction

Nanotexturing of crystalline silicon (c-Si) surfaces has been extensively investigated in the past and recent years by applying texturing techniques like reactive ion etching [1,2], plasma-chemical etching [3–5], metal-assisted electrochemical etching [6,7] and laser-assisted texturing [8]. Significant progresses made in optimization of the cell process for nanotextured cells have led towards high conversion efficiencies [6,9]. Very low surface reflection values can be reached for mono c-Si wafers by the formation of black silicon (B-Si) texture, which opens tremendous potential of an improvement in short-circuit current density (J_{sc}) of the solar cells. Multicrystalline silicon (mc-Si) solar cells are supposed to benefit strongly by the application of nanotexturing process because a relatively higher optical loss of an acidic textured surface is one of the main reasons for its overall much lower efficiency in comparison to typical mono c-Si solar cells. Nanotexturing approach for mc-Si surfaces is therefore supposed to enhance the overall cell performance by significantly minimizing the optical losses.

We recently proposed a F_2–based atmospheric pressure dry etching (ADE) process that combines the cost-effectiveness of a plasma-less atmospheric pressure dry texturing process with an industrial high-throughput inline approach promising high dynamic etch rates [10–12]. The texturing process can be effectively controlled to obtain nanostructures of different surface morphologies and low surface reflection properties. Very recently, we combined this F_2-based nanotexturing and a short post-etching process to reach 18.0% conversion efficiency (η) for mc-Si solar cells with aluminum back-surface field (Al-BSF), with an absolute gain of up to 0.3% compared to the acidic textured solar cells [13]. Other recent works have also shown significant improvement in η by forming black silicon nanotexture using metal assisted etching process [7,14] or plasma based etching methods [15,16], which is then followed by a post-etching procedure using either alkaline or acidic solutions. Although this texturing approach has already shown a promise of significantly enhancing the η of the mc-Si solar cells, a simple-one step nanotexturing process is even more attractive in both technological and economical points of view. Although such a single-step nanotexturing for mc-Si has been investigated by several groups in the past [2,3,17,18], the texturing methods used in those works are difficult to apply in an industrial scale, mainly due to economic

---

prospects (high cost of ownership) and/or environmental concerns (use of high global warming potential gases like SF_6, CF_4, NF_3).

In this paper, we present single-step plasma-less dry texturing method as an alternative method of nanotexturing the c-Si surface to achieve higher J_{sc} values. This single step texturing approach requires removal of a very low amount of Si in order to reach low surface reflection values. Such a fast etching step allows high throughput for large-scale industrial applications. Here, we discuss about the challenges imposed by this single step nanotexturing process to the subsequent solar cell process steps – especially surface passivation and emitter formation processes. The emitter formation in nanostructured surface is discussed in detail. We start the optimization of the emitter by predictive simulations of the phosphorous in-diffusion and emitter formation. The optimized emitter diffusion process is used to fabricate nanotextured mc-Si Al-BSF solar cells and the electrical characteristics are compared to that of reference acidic textured solar cells. Electron beam induced current (EBIC) method is then used to perform a microscopic characterization of the emitter and the simulated and experimental observations are used to provide insights to reach full potential of F_2-based nanotextured surface for mc-Si solar cells.

2. Surface passivation of single-step nanotextured surfaces

We use $< 100 >$, p-type, 1 Ω cm float-zone (FZ) c-Si wafers of 250 μm initial thickness in order to investigate the influence of the single-step nanotexturing process on the morphology and electrical behavior of the c-Si solar cells. All the wafers are saw-damage etched before the dry texturing process. The test wafers are dynamically etched on both sides at the set wafer temperature of 200 °C using an effective F_2-concentration of 5% applying the plasma-less atmospheric pressure dry etching (ADE) technique. Since the etching process is single sided, we first etch one wafer side and subsequently the other wafer side. Nanostructures with different surface enlargement ratios are formed on c-Si surface by varying the etching duration. The surface morphology is investigated by Scanning Electron Microscopy (SEM) (Hitachi SU-70) and the surface reflection is measured using spectrophotometer in an integrating sphere (Varian Cary 5000). The weighted surface reflection (R_w) values in the wavelength spectrum of 300–1200 nm are estimated from reflection measurements performed after the texturing process by using the IQE of a standard mc-Si solar cell under AM 1.5G spectrum [19]. The surface enlargement factor of nanostructures is estimated by Atomic Force Microscopy (Dimension 3100, Digital Instruments) using super sharp tip (Nanosensors SSS-NCH) with tip radius < 2 nm and operating in the tapping mode. Since the tip of atomic force microscope might not reach the extreme points of the deep nanostructures, the measurement should be interpreted only as the minimum value of surface enlargement factor. Fig. 1 shows the R_w values of the nanostructures formed by removing different amounts of Si during the texturing process. With an increasing amount of Si removal during the texturing process, R_w falls exponentially from $\approx 18\%$ down to $\approx 2\%$. For comparison, R_w values of the alkaline and acidic textured wafers are measured to be ≈ 10–11% and ≈ 24–27% respectively. The exponential reduction in the reflection values can be initially explained by an increase in the depth of nanostructures with an increasing duration of etching. Even longer etching duration further lowers the surface reflection of the c-Si surface and is likely to be driven by the gradual increase in density of nanostructures per unit area.

In Fig. 1, it is obvious that although the deeper nanostructures promise nearly perfect optical confinement, they leave a greatly enlarged c-Si surface behind. Deep nanostructures with very low R_w show high values of minimum surface enlargement factor of up to ≈ 2.3 in comparison to ≈ 1.3 measured for the alkaline texture
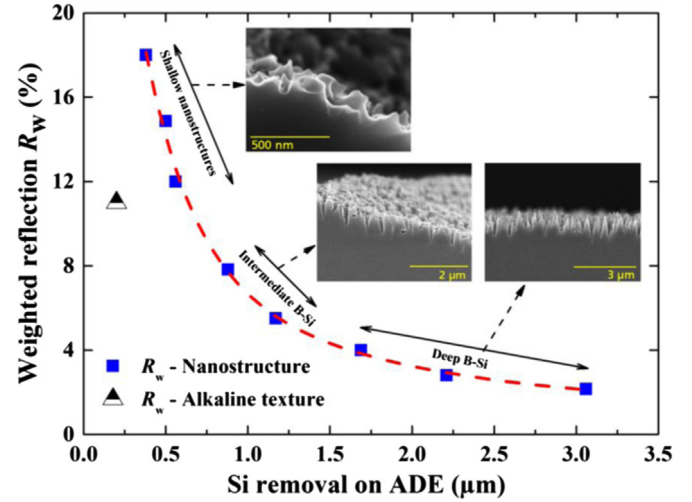

Fig. 1. Weighted surface reflection (R_w) of nanostructures formed by different amount of Si removal during the nanotexturing process. The plot in this range of the parameter variation can be very well fitted by using an exponential decay function. For comparison, R_w of alkaline textured wafer is also plotted. No coating is present on the textured surfaces.

on mono c-Si. Only the shallow nanostructures that are formed with less than ≈ 0.7 μm of average Si removal show comparable or lower minimum surface enlargement factors than the alkaline textured wafer. An increasing surface area increases the amount of surface defects/dangling bonds at the Si surface, which act like active recombination centres for the photo-generated charge carriers near the Si surface.

In order to understand the influence of surface texturing on the lifetime of minority charge carriers, symmetrical test structures are prepared on p-type, 1 Ω cm FZ c-Si wafers. The wafers are textured on both sides by using ADE process, changing the process duration to form nanostructures of different aspect ratios. After cleaning the wafers in HNO_3/HF based solution, both surfaces are then passivated by 10 nm plasma-assisted atomic layer deposited (p-ALD) AlO_x layers followed by 70 nm PECVD SiN_x layers. A stack of ALD AlO_x/PECVD SiN_x layers is chosen as it is previously observed that PECVD SiN_x alone is unable to form a conformal passivation layer in single-step nanotextured surfaces [11]. In order to emulate the standard Al-BSF solar cell fabrication process,
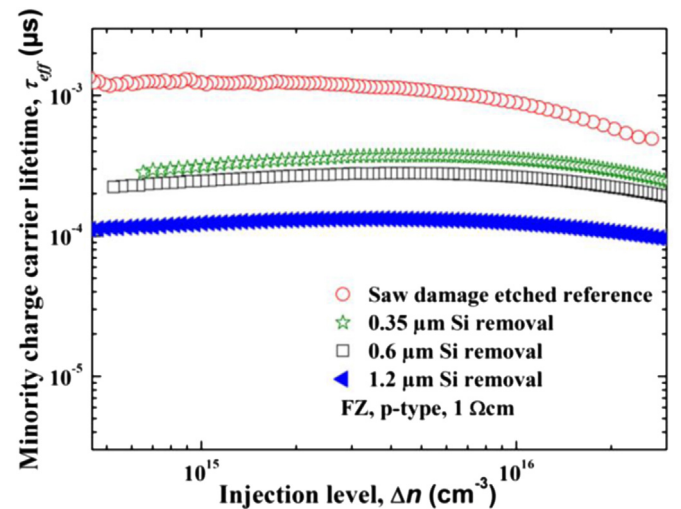

Fig. 2. Plot comparing minority charge carrier lifetimes (τ_{eff}) for symmetrically prepared saw-damage etched reference and nanostructured samples after passivation with AlO_x/SiN_x stack and fast-firing step. The injection level is the excess carrier density (Δn).

the test structures are thermally treated in a fast-firing oven at a high set peak temperature of 880 °C for an effective peak temperature duration of about 3 s. The effective lifetime of minority charge carriers (τ_{eff}) over a range of injection densities (Δn) is determined by quasi steady state photo-conductance (QSSPC) measurements. Fig. 2 shows the minority charge carrier lifetimes of nanotextures that are formed by applying different etching durations. It can be observed that an increasing amount of removed Si during the texturing process leads to an increase in surface recombination of the minority charge carriers. This can be attributed to the cumulatively larger surface area of the wafer after the dry texturing process.

3. Emitter diffusion in nanostructures

The formation of a n-type emitter in a p-type substrate is realized by a high-temperature process that includes first the deposition of phosphosilicate glass (PSG) layer on the substrate using phosphooxychloride (POCl$_3$) and oxygen (O$_2$), which is then followed by the diffusion of phosphorous atoms from the deposited PSG layer into the Si bulk (the so-called drive-in step). The sheet resistance of the n-type emitter is determined by the amount of electrically active phosphorous atoms diffused into the substrate. The surface phosphorous concentration is a very critical parameter for the contact formation between the highly doped Si and the screen printed silver. A certain level of surface P concentration is necessary in order to obtain low metal-semiconductor contact resistivity and high fill factor (FF) in a solar cell [20,21]. At the same time, too high amounts of phosphorous in the surface and emitter region activates additional surface and bulk recombination mechanisms that are driven by defect assisted recombination (Shockley-Read-Hall) and Auger recombination. The standard n-type emitter profiles are therefore designed in a way to possess as less phosphorous atoms as possible that, however, still contains enough phosphorous atoms necessary to ensure a low specific contact resistivity. The emitter depth has to be carefully chosen to ensure that it is shallow enough to avoid longer path lengths for the photo-generated charge carriers in the emitter region before their collection, and in the same time deep enough to avoid shunting problems that can occur due to spiking of Ag into the space charge region during contact firing process.

The unique morphology of the nanotextured surfaces presents additional challenges to control the doping profile of the emitter. Deposition of PSG layers on the nanostructures during the first step of emitter diffusion process plays a crucial role in defining the emitter profile. Fig. 3(i) shows a SEM image of the nanotextured c-Si surface where the nanostructures are entirely covered with PSG layers formed during the first phase of the emitter diffusion process. Fig. 3(ii) gives an impression of our expectation of the diffusion of phosphorous atoms from PSG layers during the drive-in step of the emitter diffusion process in nanotextured surface. The deposited PSG layer acts like many limited point diffusion sources during the drive-in step. In comparison to a flat surface, a nanotextured surface has much higher volume of PSG per unit wafer area available for the drive-in step. This leads to the diffusion of higher number of phosphorous atoms into the nanotextured surface in comparison to the non-textured surface. Fig. 3(iii) compares the emitter sheet resistance (R_{sh}) values measured for nanotextured surfaces and the reference non-textured (saw-damage etched) surface after the diffusion process that is aimed to reach $R_{sh} \approx 75 \ \Omega/\square$. R_{sh} values are measured by both inductive coupling and four-point probe measurement methods. The four point probe measurement is performed by measuring the complete wafer area with equidistant 100 points whereas the inductive coupling measurement is performed for 3 columns of about 20 measurement points in the middle section of the wafer area
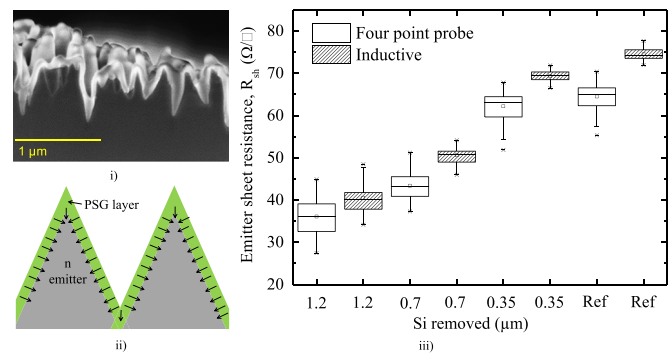

Fig. 3. (i) SEM image showing conformal deposition of PSG layers on nanotexture during the emitter diffusion process, (ii) an impression of heavy diffusion of phosphorous from the deposited PSG layers in nanotexture, (iii) comparison of emitter sheet resistances (R_{sh}) for nanotextured surfaces and the reference non-textured (saw damage etched) surface after emitter diffusion process aiming 75 $\Omega/\square$ on a saw damage etched surface. R_{sh} is determined by means of inductive coupling as well as by using four point probe technique.

[22]. Here, the four point probe method has therefore a higher spatial resolution over the inductive coupling method.

Regardless of the surface texture, the mean R_{sh} values measured by the four point probe method are slightly lower in comparison to that of inductive coupling method. Furthermore, the deviation between two methods also seems to increase for higher emitter sheet resistances. Such an underestimation of the R_{sh} measurement by the four point probe method on rougher surfaces is previously attributed to an increase in contact resistance between the voltage probe tips and the Si wafer [22]. In comparison to the four point probe method, inductive coupling is a contactless method of measuring R_{sh} of textured surfaces where the R_{sh} is derived from a measurement of the wafer resistivity before and after the emitter diffusion process [22,23]. Since the same wafer is measured before and after the diffusion process, the roughness of the wafer is expected not to have a significant influence in the measurements.

Mean R_{sh} values for nanotextured samples are lower than that of the reference non-textured samples. Moreover, the R_{sh} values gradually decrease with an increase in Si removal during the texturing process. The nanotexturing process, that requires in average only 0.35 μm of Si removal, reaches mean R_{sh} values that are close to those measured for the reference non-textured wafers ($R_{sh} \approx 75 \ \Omega/\square$). The nanotexture formed after removing 1.2 μm of Si in average, shows much lower mean $R_{sh} \approx 35 \ \Omega/\square$. From these observations, it is evident that the nanotextured surface is likely to have a higher overall doping because of an enlarged surface in comparison to the tradiional wet-chemically formed texture. Such a highly doped emitter leads to the fast recombination of the light generated charge carriers in the emitter region of the solar cell. The recombination related losses in the emitter eventually limit the photo-current generation and open circuit voltage of the solar cell. Therefore, a trade-off needs to be found between excellent light trapping and good electrical properties of a nanotextured solar cell [6,7,15,16]. In order to minimize the electrical losses due to recombination at the surface and in the emitter region, single-step nanotextures that are formed by the removal of ≈ 0.3 μm of Si during the nanotexturing process are chosen instead of deep nanostructures.

3.1. 3D simulation of emitter diffusion process in nanostructures

In order to understand the emitter formation on nanotextured surfaces, we perform 3D Sentaurus process simulations [24]. We use parameters from [25] for the phosphorous diffusion and segregation from the PSG into the Si. In the chosen model (charged pair diffusion [24]), phosphorus diffuses mainly via

PV^{2-} (diffusivity: $1.4 \times 10^{-3} \times \exp(-3.5\,\text{eV}/k_BT)$) in the highly doped silicon and via neutral (diffusivity: $0.5 \times \exp(-3.65\,\text{eV}/k_BT)$) and positively charged (diffusivity: $0.7 \times \exp(-3.482\,\text{eV}/k_BT)$) B_SSi_i pairs in lowly doped silicon. The initial phosphorus concentration ($0.9 \times 10^{21}\,\text{cm}^{-3}$) in the PSG is a gas flux dependent fitting parameter. Between Si and PSG, a segregation coefficient of $100 \times \exp(-0.4\,\text{eV}/k_BT)$ is used. The initial phosphorous concentration in the PSG is obtained by a comparison to secondary ion mass spectrometry (SIMS) and electrochemical capacitance–voltage (ECV) profiles measured on samples with planar surfaces. In order to avoid complication of addressing a stochastic surface, we assume that the nanotextured surface is comprised of periodically arranged nanoscale pyramids of 300 nm depths and uniform 300 nm peak-to-peak distances. Fig. 4(i) shows the 3D symmetry element of the nanostructure (i.e. a ¼ pyramid). For such small nanostructures, a good correlation between doping diffusion simulations and measurements was found in [26]. The phosphorous distribution for two different POCl$_3$ emitter diffusion processes (*Emitter A/B*) are simulated. In case of *Emitter A*, the initial constant source diffusion step (deposition of PSG layers on Si) followed by the limited source diffusion step (or the drive-in step) are both performed at the same temperature of 820 °C. In case of *Emitter B*, the initial constant source diffusion step is performed at a temperature that is ≈ 30 °C lower than *Emitter A* aiming for a reduction of total phosphorous concentration. This effect is further increased by intentionally adding a high amount of O$_2$ flux for *Emitter B* during the drive-in step. The drive-in temperatures for both *Emitter A* and *Emitter B* are kept identical. The drive-in step for *Emitter A* is twice as long as that for *Emitter B*. In general, *Emitter B* is designed to achieve lower doping in the nanostructures. Fig. 4(ii) shows different doping regimes in nanopyramid cross-sections after applying Sentaurus simulation of the emitter diffusion processes *A* and *B*. The simulations of an individual nanostructure suggest that irrespective of the emitter diffusion process applied, a reasonably planar depletion layer is formed well below the nanostructures. In both cases, the P concentration in the nanostructure falls steadily from the peak to the bottom resulting in a very highly doped nanostructure. However, in the case of *Emitter A*, the highly doped region (Total $[P] > 10^{20}$ cm^{-3}) extends much deeper into the nanostructure in comparison to the *Emitter B*. Also, as expected, the depletion region sinks deeper into the Si substrate in case of *Emitter A*. In the emitter diffusion process, the deposition of PSG layer is heavily influenced by the deposition temperature and a lowering

of R_{sh} is expected for an increasing deposition temperature. A lower deposition temperature leads to the deposition of PSG layers with a lower amount of phosphorous atoms. A maximum phosphorous amount that can be diffused in the drive-in process is therefore limited to the amount of phosphorous, which is available in the PSG layer.

The addition of O$_2$ flux during drive-in is expected to change the first tens of nanometers of emitter surface region, thus helping to reduce the total surface doping concentration. Fig. 4(iv) shows ECV profiles measured in plain surfaces for *Emitter B* after performing a variation of O$_2$ flux during drive-in. Linear increment in R_{sh} is observed for an increment in O$_2$ flux. This is driven by a gradual reduction of surface phosphorous concentration (N_{sh}) as well as by the decreasing depth of the highly doped region of the emitter. Since the drive-in temperatures for *Emitter A* and *Emitter B* are kept identical, difference in the amount of total phosphorous atoms between these two emitters can be mostly accredited to the difference in deposition temperature and availability of additional O$_2$ flux during the drive-in process. Particularly in this case, a high O$_2$ flux during drive in seems to be the dominant factor as *Emitter B* with no O$_2$ flux yielded $R_{sh} \approx 78\,\Omega/\square$ that is very close to that of *Emitter A* ($R_{sh} \approx 75\,\Omega/\square$). The difference in depths of the depletion layer between *Emitter A* and *Emitter B* is most likely due to the difference in drive-in durations for two emitter diffusion processes.

In general, the dopant profiles calculated from different sections of the pyramid differ considerably and therefore result in different values of R_{sh} at different points in the simulated nanopyramid structure. Fig. 4(iii) shows the top view of a section of pyramid structure after emitter diffusion process (*Emitter B*) with different colors representing different R_{sh} values and the dashed line representing the pyramid edge. It can be seen that the nanopyramid has lower R_{sh} values along the pyramid edge, which is basically due to diffusion of phosphorous from two sides (planes) of the pyramid.

Fig. 5 compares simulated emitter depth profiles considering either top, side or bottom positions of the nanopyramid structure as the initial (or zero) position of the emitter doping profile. For the nanopyramid structure, the doping profiles are plotted in the direction that is normal to the imagined planar surface. For comparison, the emitter doping profiles of the corresponding emitters on planar surfaces measured by the ECV and/or the SIMS techniques are also shown. The simulated doping profile on a planar surface (Total [P]_planar) is also plotted in Fig. 5(i), which shows a
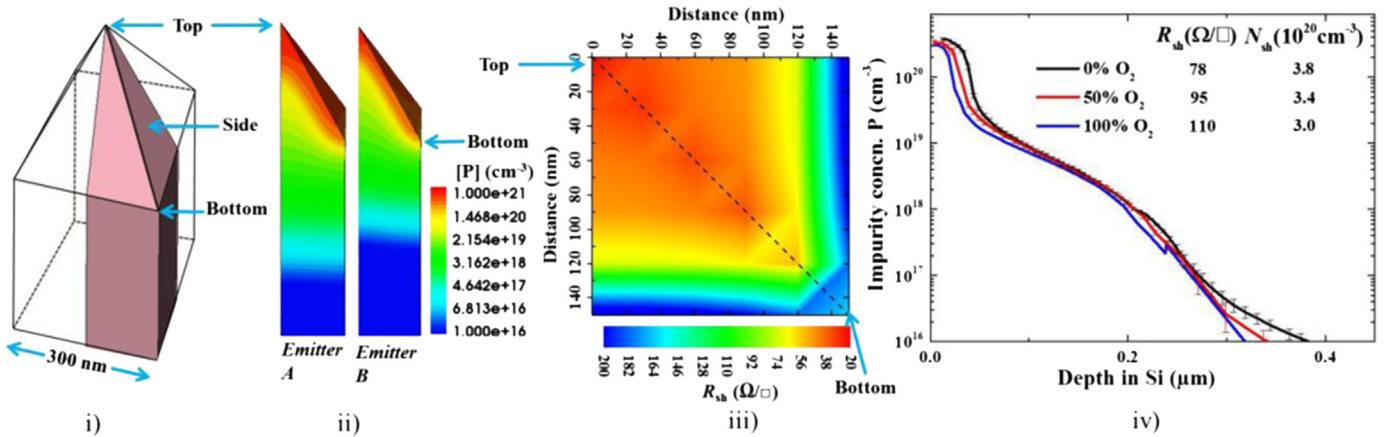

Fig. 4. (i) Simulated nanostructure geometry element, (ii) process simulation after the application of two different emitter doping processes on nanostructures showing a pyramid cross-section with different doping regimes in a nanostructure and the depletion region depth/junction depth, (iii) top view of a section of pyramid after emitter diffusion process (*Emitter B*) with mapping of simulated sheet resistance (R_{sh}) values at different pyramid locations, and (iv) Emitter diffusion profiles determined by ECV measurements on saw-damage etched surfaces for *Emitter B* after a variation of O$_2$ flux during the drive-in step.
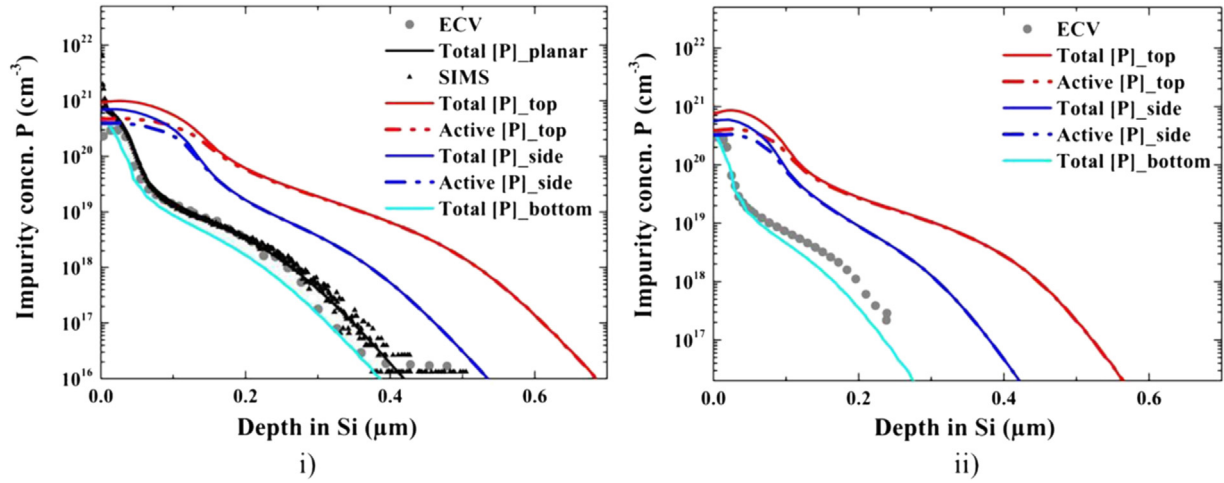
Fig. 5. Experimentally measured and simulated emitter diffusion profiles from different positions of nanostructure for (i) *Emitter A* and (ii) *Emitter B*. Total [P] and Active [P] represents the total phosphorous concentration and the electrically active phosphorous concentration respectively. Pyramid top, pyramid side and pyramid bottom represents the initial position in the nanostructure from where the dopant profiles are plotted in the direction normal to the imagined planar surface (see Fig. 4(i)). Total [P] _planar is the simulated profile of a non-textured planar surface. ECV and SIMS emitter profiles measured on a planar surface are also plotted for comparison.

good agreement to the measured SIMS profile of the same emitter diffusion process.

The process simulation of the nanostructure suggests the presence of much higher phosphorous concentration in the near-surface emitter region as well as formation of deeper depletion region in comparison to the emitter diffusion process in a flat surface. For both emitters, the simulated active surface phosphorous concentration at the top of the nanostructure (Active [P] _top) is not significantly different to the ECV profile measured for a flat reference. However, going deeper into the Si, both total concentration (Total [P]_top) and active concentration (Active [P]_top) diffusion profiles diverge significantly from the diffusion profile measured in a non-textured sample. A comparison of the simulated profiles for Total [P]_top and Active [P]_top also suggests that a significant amount of inactive phosphorous possibly exists in the nanostructure. The diffusion profiles also suggest that the diffusion of *Emitter A* leads to a higher amount of total phosphorous concentration in the nanostructure in comparison to *Emitter B*. We believe that this is related to a higher deposition temperature and most importantly to an unavailability of O_2 flux during the drive-in step of *Emitter A*. In particular, consumption of Si due to the presence of O_2 flux during the drive-in step of the emitter diffusion process is also believed to have a dominant effect in the lowering of inactive phosphorous concentration in the nanostructure.

Irrespective of the doping process; it is observed that the simulated phosphorous doping profile from the bottom part of the pyramid structure (Total [P]_bottom) correlates very closely to the measured ECV profile of the planar reference Si wafer for the same emitter diffusion process parameters. This can be explained by the following. The effective diffusivity of phosphorous in Si is dominated by the temperature and therefore is almost constant in the nanostructure. Since the PSG layers are conformally grown in the peak as well as in the valleys of the texture (see Fig. 3(ii)); the finite doping sources in the PSG layer leads to the phosphorous diffusion in several directions into the Si, both at the peak and at the bottom of the pyramid. Such a multi-dimensional diffusion leads to the formation of depletion region in such a way that the distance of the depletion region from the lowest point of the nanotexture is close to the depletion region depth in a non-textured surface. In the final section of this paper, we would experimentally verify these simulation results by the help of EBIC measurements.

3.2. Application of single-step nanotexturing for mc-Si based solar cells

Surface texturing of mc-Si wafers possesses different challenges compared to mono c-Si wafers due to the presence of crystal grains with different crystal orientations and defects at grain boundaries. Due to the absence of any energetic ions in the process, the F_2 based atmospheric pressure texturing is solely a chemical process and is mainly driven by the thermal energy provided to the wafer substrate. Based on SEM images, we found that the texturing process is slightly different for different crystal orientations. Texturing conditions in mono c-Si wafers are therefore not necessarily transferrable to the mc-Si wafers. A deeper investigation on this topic will be presented elsewhere. Nevertheless, it is possible to decrease an overall surface reflection in all grains of the mc-Si wafer by the formation of nanostructures of varying surface enlargement factors.

In this section, we would like to present the application of the optimized emitter diffusion process on single-step nanotextured solar cells (hereby *S-Nanotexture*). For the relative comparison, we also present here the solar cell results of our two-step nanotexturing process (*M-Nanotexture*) that previously showed an improved solar cell performance to the acidic texture [13]. Since the *S-Nanotexture* and *M-Nanotexture* are processed independently with wafers taken from separate ingots, only a relative comparison of electrical performance between two solar cell batches is possible. Fig. 6(i) outlines the Al-BSF solar cell process that was followed for both nanotextured and acidic textured wafers. 15.6×15.6 cm^2 p-type mc-Si wafers with 3 Ω cm base resistivity are first saw-damage etched in acidic solution before performing the nanotexturing process. A F_2 based dry texturing tool [10–12] is used to form nanotexture at the set wafer temperature ($T_{wafer} > 150$ °C) and using an effective F_2-concentration of 5%. For *S-Nanotexture*, the process duration is varied in order to remove ≈ 0.3 µm of Si in average. For *M-Nanotexture*, the process duration is varied to remove ≈ 1.5 µm of Si in average to form deep nanotexture, and then shortly dipped in alkaline solution for a controlled duration to remove further ≈ 0.6 µm of Si. This two-step etching process enables reduction of the overall surface area of deep nanotexture and also allows conformal deposition of PECVD layers. After RCA cleaning [27], nanotextured and acidic textured wafers are subjected to the tube emitter diffusion process, *Emitter A*, with a known $R_{sh} \approx 75$ $\Omega/\square$ in saw-damage etched (non-textured) wafers. As shown in Fig. 3(iii),
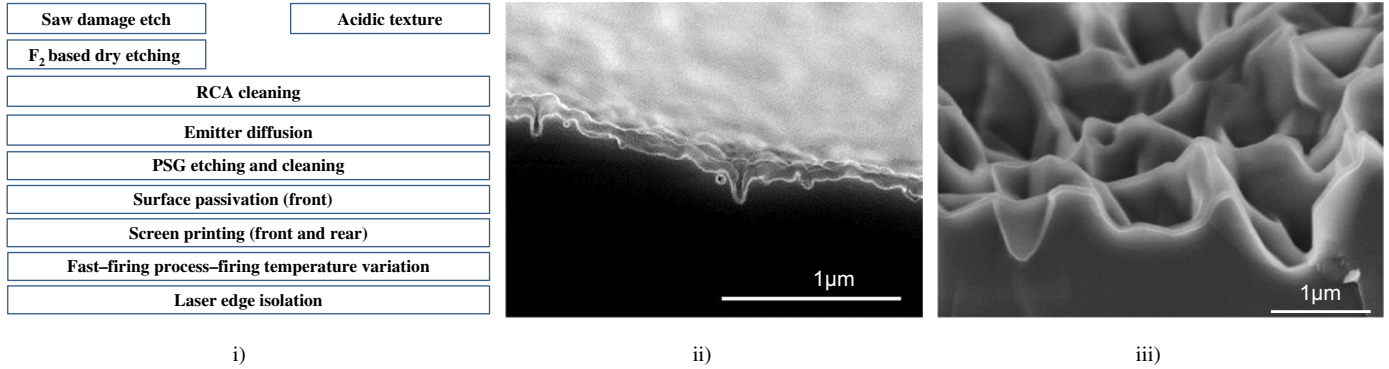
Fig. 6. (i) Process flow for the Al-BSF solar cell process featuring acidic texture, *S-Nanotexture* and *M-Nanotexture*, (ii) SEM image of *S-Nanotexture* after surface passivation with ALD AlO$_x$ and PECVD SiN$_x$ layer, and (iii) SEM image of *M-Nanotexture* after surface passivation with PECVD SiN$_x$ layer.

such an emitter diffusion process results in lower R_{sh} values in nanotextured surfaces. Therefore, a group of nanotextured wafers are diffused with the modified emitter diffusion process, *Emitter B*. As explained in Section 3.1, *Emitter B* is intended to lower the total phosphorous concentration in the near-surface emitter region of the nanotexture so as to reach emitter sheet resistances that are close to $R_{sh} \approx 75 \, \Omega/\square$. After the emitter diffusion process, the textured side is deposited with dielectric passivation layers. *S-Nanotexture* is passivated by depositing a stack of 10 nm plasma assisted atomic layer deposited (p-ALD) AlO$_x$ layer and PECVD SiN$_x$ layer. ALD layer deposition has been already known to provide good surface passivation of *S-Nanotexture* [11]. The conformal AlO$_x$ layer deposited on an enlarged surface significantly lowers the interface defect density (D_{it}) by maintaining an excellent Si–SiO$_x$ interface [28]. On the other hand, a high amount of fixed negative charges present in the AlO$_x$ layer [28–30] is also expected to deteriorate the passivation of n$^+$ surfaces after a certain level of surface doping [28]. However, applying a firing process on AlO$_x$/SiN$_x$ stack is reported to significantly lower the density of negative charges in AlO$_x$ layer, thereby providing an excellent chemical passivation of n$^+$ surfaces irrespective of the surface doping [31]. Meanwhile, adaptation of PECVD dielectric layers on *S-Nanotexture* is also a matter of ongoing investigations. In contrast, *M-Nanotexture* can be very well passivated by depositing only PECVD SiN$_x$ layer [13]. After the surface passivation step, *M-Nanotexture* wafers are screen-printed with Ag front-grid and rear Al with solder pads; and fired using an industrial fast-firing oven. *S-Nanotexture* wafers are screen printed to form four separate Ag grid patterns of 5 cm × 5 cm whereas the rear side is fully printed with Al paste. The *S-Nanotexture* wafers are eventually separated into four individual solar cells before the firing process. For both group of wafers, fast-firing is followed by laser edge isolation of individual solar cells. The average weighted surface reflection values (R_w) measured after diffusion of *Emitter A* and PECVD SiN$_x$ deposition are 8.3% for acidic texture, 5% for *S-Nanotexture* and 4.4% for *M-Nanotexture* surfaces.

Fig. 6(ii) shows the SEM image of *S-Nanotexture* passivated with AlO$_x$/SiN$_x$ passivation stack. For comparison, SEM image of *M-Nanotexture* passivated with SiN$_x$ layer, is also shown in Fig. 6(iii). *IV* measurements of the finished *S-Nanotexture* solar cells and the acidic texture solar cells are carried out and the results of the best cells are listed in Table 1. The IV characteristics of the *S-Nanotexture* solar cells are also compared to our previously reported *M-Nanotexture* solar cells.

Both types of nanotextured solar cells with *Emitter A* show similar J_{sc} values to the acidic textured solar cells of the same solar cell batch. However, nanotextured solar cells with *Emitter B* show a significant improvement of J_{sc} in comparison to the acidic textured solar cell. An improvement in $J_{sc} \approx 0.7 \, mA/cm^2$ to the acidic texture with *Emitter A* is achieved for *S-Nanotexture* with *Emitter*

B. The J_{sc} improvement achieved is similar to the one previously achieved for the *M-Nanotexture* solar cell with *Emitter B* (0.8 mA/cm^2) that was first textured by F$_2$ based nanotexturing and then modified by an additional alkaline post-etching process. Therefore for *S-Nanotexture*, this increase in J_{sc} implies that $\approx 0.3\%$ absolute gain in η to the acidic texture is possible for comparable V_{oc} and FF values. In general, this whole batch of solar cells (both *S-Nanotexture* and acidic texture) shows lower conversion efficiencies than the solar cell batch featuring *M-Nanotexture*, mainly due to a lower FF. We believe that a non-optimized firing process used for these solar cells with smaller edge length is responsible for this effect.

Fig. 7(i) compares the surface reflection (R) and internal quantum efficiency (IQE) at 400 nm, specific contact resistivity of the front contact (ρ_C) and emitter sheet resistance (R_{sh}) for the solar cell batch featuring acidic texture, *S-Nanotexture* and *M-Nanotexture*. ρ_C is measured by Transmission Line Method (TLM) and R_{sh} is calculated from the slope of the linear plot obtained for the resistance measured between the adjacent contacts and their corresponding distances [32,33]. Low $\rho_C \leq 3 \, m\Omega \, cm^2$ close to that of acidic texture are measured for both types of nanotextured surfaces that are diffused with *Emitter A*. In comparison to *M-Nanotexture*, however, *S-Nanotexture* with *Emitter B* shows lower FF mainly due to a comparatively higher ρ_C value. Since *Emitter B* consists of high enough surface phosphorous concentration that is required to allow good Ag–Si metallic contacts, we believe that a non-optimized firing process is possibly the main reason for a higher ρ_C in case of *S-Nanotexture* diffused with *Emitter B*. The firing process could have also negatively influenced the surface passivation layers and resulted in V_{oc} losses for *S-Nanotexture* despite using a stack of ALD AlO$_x$/PECVD SiN$_x$ for surface passivation. Another plausible explanation for a lower V_{oc} is a high recombination of charge carriers in the emitter region of the *S-Nanotexture*. However, since the V_{oc} of *S-Nanotexture* does not significantly change from *Emitter A* to *Emitter B*, the losses seem to come mainly from surface passivation. Therefore, despite possessing a higher J_{sc} value to the acidic texture, the overall efficiency of *S-Nanotexture* with *Emitter B* suffers mainly due to lower V_{oc} and FF values. Further optimizations in surface passivation and contact formation processes promise an improvement of the conversion efficiency of *S-Nanotexture* to the same level as *M-Nanotexture*. Fig. 7(ii) shows the internal quantum efficiency (IQE) and reflection (R) measurements of the fabricated solar cells and compares them to that of *M-Nanotexture*. It should be noted that application of *Emitter B* significantly increases the surface reflection of *S-Nanotexture* in comparison to *Emitter A* at short wavelengths. This effect is mainly due to the presence of high amount of O$_2$ flux during the drive-in step of *Emitter B* that oxidizes the fine structures of *S-Nanotexture*. In comparison, no significant change in

Table 1
IV Measurements of two separate batches of solar cells featuring an Al-BSF with different edge length. ΔJ_{sc} represents the J_{sc} improvement achieved in comparison to the acidic textured solar cells with *Emitter A* that were fabricated in the same batch. It should be noted that only a relative comparison is possible between two solar cell batches.

| Edge length (mm)	Surface passivation	Best cells	V_{oc} (mV)	J_{sc} (mA/cm^2)	η (%)	FF (%)	ΔJ_{sc} (mA/cm^2)
50	AlO$_x$/SiN$_x$	Acidic texture, *Emitter A*	627	35.1	17.2	78.2	–
50	AlO$_x$/SiN$_x$	*S-Nanotexture, Emitter A*	618	35.2	17.2	78.8	+0.1
50	AlO$_x$/SiN$_x$	*S-Nanotexture, Emitter B*	619	35.8	17.0	76.5	+0.7
156	SiN$_x$	Acidic texture, *Emitter A*	627	34.9	17.7	80.7	–
156	SiN$_x$	*M-Nanotexture, Emitter A*	626	34.9	17.7	81.0	+0.0
156	SiN$_x$	*M-Nanotexture, Emitter B* [13]	627	35.7	18.0	80.4	+0.8
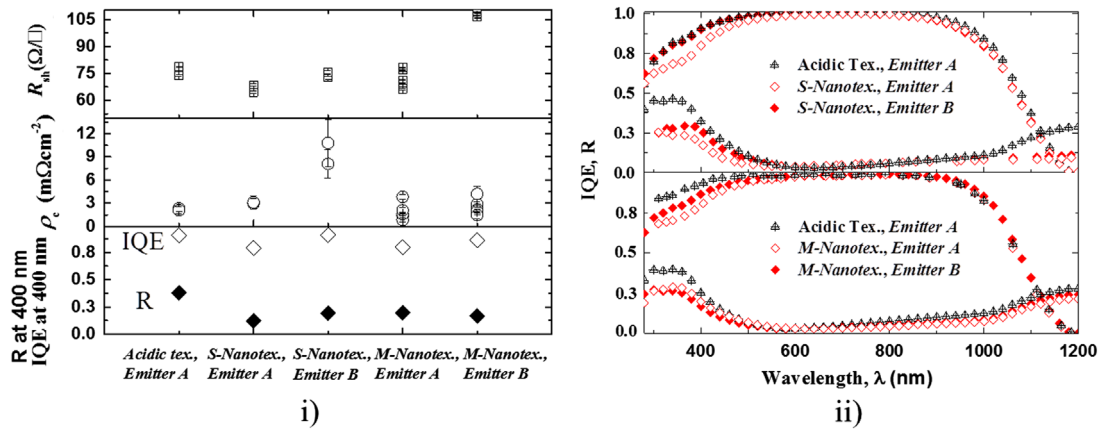
Fig. 7. (i) Plot comparing the effects of different emitter diffusion processes and surface topographies on R_{sh}, ρ_C, IQE and R, of the Al-BSF solar cell batch featuring acidic texture, *S-Nanotexture* and *M-Nanotexture*, (ii) IQE and reflection measurements of the reference and *S-Nanotexture* solar cells in comparison to *M-Nanotexture* solar cells. For both types of nanotextured solar cells, the plotted IQE represents an area averaging surface reflection of multiple grains in the middle section of the wafer.

surface reflection is observed between *Emitter A* and *Emitter B* processes in the case of *M-Nanotexture*.

IQE measurements are crucial to understand the electrical behavior of solar cells. It can be seen that despite having lower surface reflection, the IQE at short wavelengths for both types of nanotextured solar cells with *Emitter A* are significantly lower than for the acidic textured solar cell. Application of *Emitter B* significantly lowers the emitter recombination in nanotextured solar cells, which is reflected in an enhanced IQE in comparison to that of *Emitter A*. Identical conclusions of an improvement in IQE after using high sheet resistance emitter are previously attributed to the reduction of Auger recombination in the emitter [6]. A combination of *S-Nanotexture* and *Emitter B* show equivalent blue response in comparison to the acidic texture diffused with *Emitter A*. Although showing an improvement in IQE signal, if compared to the combination of *Emitter A* and *M-Nanotexture*, one could observe that a combination of *Emitter B* and *M-Nanotexture* still show some losses in blue spectrum of wavelength in comparison to the acidic texture with *Emitter A*. Therefore, a dedicated optimization of emitter diffusion process is necessary for even a slight change in surface texture. On the application of *Emitter B*, a slightly higher IQE is observed for *S-Nanotexture* in comparison to *M-Nanotexture*. This is mainly due to higher emitter recombination losses in *M-Nanotexture* as it consists of deeper features and thus an overall larger surface area (see Fig. 6(ii) and (iii)). Increase in emitter recombination due to an enlarged surface area limits the lifetime of the photo-generated charge carriers [34]. In addition, surface and emitter recombination is believed to be further worsened by the formation of a deeper pn-junction in nanotextured surfaces (see Fig. 4). This leads to fast recombination of minority charge carriers generated in the upper regions of the texture on their way to the space charge region (SCR). This ultimately worsens the collection probability and is visualized as losses in the IQE of the solar cell.

3.3. Electron beam induced current measurements of nanotextured surfaces

In order to investigate the junction depth of the nanotextured solar cells, we perform electron beam induced current (EBIC) measurements. The EBIC method is widely used in semiconductor analysis and is based upon measurement of the external current flow between differently doped regions in the semiconductor, when it is exposed to the electron beam inside a scanning electron microscope. In a solar cell, the charge carriers generated by the electron beam separate in the space charge region (SCR) of the pn-junction and hereby cause flow of an external current through the metal contacts. With neglecting influences of crystal defects or surfaces, this results in a current gradient with a maximum at the position of the SCR. The maximum EBIC signal therefore can be used to locate the p–n junction of a device. The detailed description of the measurement technique can be found elsewhere [35]. As pointed out by Kluska et al. [36], while EBIC signal measured at a particular location depends both upon local collection probability as well as upon local generation rate; topographical features and surface damages also strongly affect the generated EBIC signal. In general, regions of relatively higher recombination can cause a shift of the EBIC maximum, which then does not represent the position of the space charge region any longer. A large surface with a recombination velocity that is higher than that of the bulk underneath the SCR could shift the EBIC maximum deeper towards the bulk material and therefore erroneously indicate a deeper junction depth. The nanotextured sample consists of an enlarged surface area with higher surface recombination probability, which could affect the EBIC signal maximum. Although an excellent surface passivation by ALD Al$_2$O$_3$ layer is supposed to significantly minimize the recombination effects on EBIC signals, nevertheless, the measured EBIC maximum has to be interpreted as the maximum depth of the SCR. Use of mc-Si samples could also
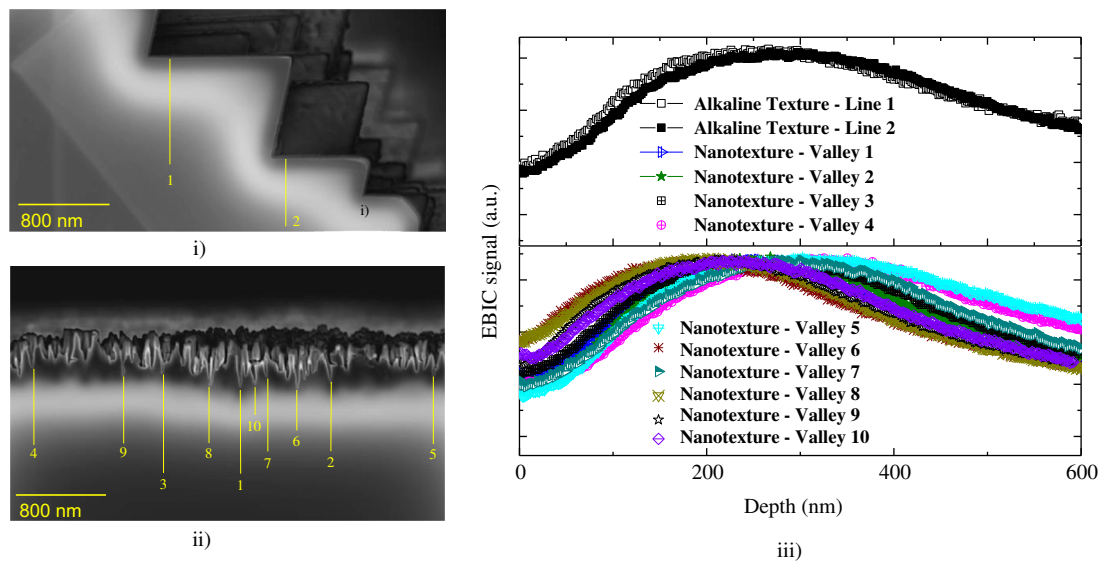
Fig. 8. SEM image with added EBIC signal of the (i) Cz mono c-Si reference wafer with alkaline texturing, (ii) of the Cz test-wafer with deep nanotexture; and (iii) Plot of the EBIC line scan of reference and test wafers that received identical emitter diffusion process (*Emitter A*).

influence EBIC signals due to crystal dislocations, defects, grain boundaries and also non-uniform diffusion of dopants in different grains [37]. In order to obtain a distinct EBIC signal free from those effects, acidically polished $<100>$, p-type mono c-Si (Cz) test samples of 200 μm initial thickness are used as test wafers. The EBIC measurement samples are prepared by performing deep nanotexturing, diffusion of *Emitter A* that is followed by all of the later steps that are identical to those used to prepare *S-Nanotexture* mc-Si solar cells in Section 3.2. Fig. 8 compares the EBIC signal of the alkaline textured and nanotextured mono c-Si samples. In order to reduce a disturbing influence of the smaller generation volume at the top of the pyramids on the EBIC signals [36], the line scan for alkaline textured sample is taken from the side edge of the pyramid. In the case of nanotextured sample, the depth where the EBIC maximum signal occurs is measured from the deepest point of several valleys. It is observed that the EBIC maximum values can be found in a depth range of 200–350 nm, which is in good agreement with the depth measured for the alkaline textured reference. Meanwhile, a slight variation of EBIC maximum values is observed for different line-scans performed in the nanotextured sample. This could be either due to the influence on the EBIC signal by the presence of micron-scale valley-like structures that are present at the Si surface after the acidic polishing step, and/or due to the uncertainties in setting the starting point of the line-scan. Additionally, the depths of the EBIC maximum measured for alkaline texture from the surface and for the nanotexture from the deepest point are comparable to each other. This supports the finding that the valleys of nanostructures can be interpreted as point-like dopant sources.

This also confirms the formation of a deeper pn-junction in nanotextured solar cells (if the depth is measured from texture tips) and experimentally verifies the results that we obtained from the predictive simulations of these structures. In Fig. 8(i), one should notice that the EBIC maximum closely follows the microstructures like pyramidal texture thereby inducing non-homogeneities in the depletion layer. Interestingly in the nanotextured surface, a relatively flat pn-junction is formed underneath the nanostructures. As the EBIC maxima follow the nanostructures as well, several local non-homogeneities in the EBIC image of nanotexture (see Fig. 8(ii)) are also observed. The differences in the feature sizes of the nanotexture is expected to lead to slight differences in the doping levels at certain depths below the nanotexture. The locally non-uniform EBIC

signal therefore suggests the formation of locally non-homogeneous SCR below the nanotexture. Such a SCR with larger effective area is likely to enhance the minority charge carrier recombination. Based on similar observations, Shen et al. [38] suggested that in addition to the vertical electric field perpendicular to the original wafer surface, a lateral electric field (parallel to the originally flat wafer surface) is introduced in case of nanotextured surfaces and this ultimately results in higher reverse saturation current density (J_{02}) and a low shunt resistance (R_{shunt}) value in nanotextured solar cells. However, we do not observe any effect of such locally non-homogeneous EBIC maxima in the electrical properties of our nanotextured solar cells. The emitter saturation current density (J_{02}) and parallel shunt resistance (R_{shunt}) values that are calculated from the dark *IV* measurements show no significant differences to those of the reference wet-textured solar cells. One possible explanation could be that the surface enlargement factors of the nanotexture applied in our mc-Si solar cells are not very large in comparison to that of traditional wet-chemical texturing techniques. Therefore, the share of the electric field that is parallel to the wafer surface is small enough not to affect the electrical parameters of the solar cells. Therefore we conclude that the losses in IQE were mainly caused by the Auger recombination in the emitter as also previously concluded by other works [6,7,14,15,34] that, however, is also aided by the formation of a deeper pn-junction than in wet-chemically textured surfaces.

4. Conclusion

In this paper, we mainly studied the emitter formation process in single-step nanotextured c-Si surfaces that are prepared by atmospheric pressure dry etching process. We performed predictive simulations of emitter diffusion process in a nanostructure that suggested the presence of very highly doped areas near the nanostructure surface, which also extends deeper into the nanostructure. The simulations suggest that the deposition temperature and most importantly the availability of a considerable amount of O_2 flux during the drive-in step have a determining effect on the doping profile of the nanostructures. The emitter diffusion process leads to the formation of a relatively planar pn-junction below the nanostructures. For an identical emitter diffusion process, the simulated dopant profile, if measured from the bottom of nanotexture follows the ECV profile of the emitter measured in a flat reference. EBIC

signals are also used to determine the junction depth in the nanostructured Si and the experimental results lead to the similar conclusions obtained from the process simulation. We applied the optimized emitter diffusion process on the nanotextured surfaces in order to improve the IQE of single-step nanotextured solar cells to the equivalent level of the acidic textured solar cell. In comparison to acidic texturing, we achieved significant improvement in J_{sc} by applying both one-step and two-step nanotexturing processes. Further reduction of recombination in surface and emitter region; and optimization of contact formation process is expected to increase the conversion efficiency of both types of nanotextured solar cells to higher values in comparison to acidic textured solar cells.

Acknowledgment

References

[1] K. Fukui, Y. Inomata, K. Shirasawa, Surface texturing using reactive ion etching for multicrystalline silicon solar cells, in: Proceedings of the Photovoltaic Specialists Conference, Conference Record of the Twenty-Sixth IEEE, Anaheim, 1997, pp. 47–50.

[2] K.-s Lee, M.-H. Ha, J.H. Kim, J.-W. Jeong, Damage-free reactive ion etch for high-efficiency large-area multi-crystalline silicon solar cells, Sol. Energy Mater. Sol. Cells 95 (2011) 66–68.

[3] J. Rentsch, N. Kohn, F. Bamberg, K. Roth, S. Peters, R. Lüdemann, R. Preu, Iso-tropic plasma texturing of mc-Si for industrial solar cell fabrication, in: Proceedings of the 31st IEEE Photovoltaic Specialists Conference, Orlando, Florida, 2005, pp. 1316–1319.

[4] J.S. Seiffe, Plasma-based surface modification technologies for crystalline silicon photovoltaics, in: Universitätsbibliothek Freiburg, 2013.

[5] H.F.W. Dekkers, G. Agostinelli, D. Dehertoghe, G. Beaucarne, Improved performances of mc-Si solar cells by isotropic plasma texturing, in: Proceedings of the 19th European Photovoltaic Solar Energy Conference, WIP-Munich, ETA-Florence, Paris, France, 2004, 412–415.

[6] J. Oh, H.-C. Yuan, H.M. Branz, An 18.2%-efficient black-silicon solar cell achieved through control of carrier recombination in nanostructures, Nat. Nanotechnol. 7 (2012) 743–748.

[7] X.X. Lin, Y. Zeng, S.H. Zhong, Z.G. Huang, H.Q. Qian, J. Ling, J.B. Zhu, W.Z. Shen, Realization of improved efficiency on nanostructured multicrystalline silicon solar cells for mass production, Nanotechnology 26 (2015) 125401.

[8] S. Kontermann, T. Gimpel, A.L. Baumann, K.-M. Guenther, W. Schade, Laser Processed Black Silicon for photovoltaic applications, in: Silicon PV, Leuven, 2012.

[9] P. Repo, J. Benick, V. Vähänissi, J. Schön, G.v. Gastrow, B. Steinhauser, M.C. Schubert, M. Hermle, N-type black silicon solar cells, in: Silicon PV, Hamelin, 2013.

[10] B. Kafle, J. Seiffe, M. Hofmann, L. Clochard, E. Duffy, J. Rentsch, Nanostructuring of c-Si surface by F$_2$-based atmospheric pressure dry texturing process, Phys. Status Solidi A 212 (2015) 307–311.

[11] B. Kafle, D. Trogus, B. Dresler, D. Köhler, G. Mäder, L. Clochard, E. Duffy, M. Hofmann, J. Rentsch, Industrial screen-printed solar cells with novel atmospheric pressure dry texturing process, in: Proceedings of the 28th EUPVSEC, WIP Munich, ETA-Florence, Paris, 2013.

[12] B. Dresler, G. Mäder, D. Köhler, L. Clochard, E. Duffy, B. Kafle, M. Hofmann, J. Rentsch, Novel industrial single sided dry etching and texturing process for silicon solar cell improvement, in: 27th EUPVSEC, Frankfurt, 2012, pp. 1825–1828.

[13] B. Kafle, A. Mannan, T. Freund, L. Clochard, E. Duffy, M. Hofmann, J. Rentsch, R. Preu, Nanotextured multicrystalline Al-BSF solar cells reaching 18% conversion efficiency using industrially viable solar cell processes, Phys. Status Solidi (RRL) – Rapid Res. Lett. 9 (2015) 448–452.

[14] X. Ye, S. Zou, K. Chen, J. Li, J. Huang, F. Cao, X. Wang, L. Zhang, X.-F. Wang, M. Shen, X. Su, 18.45%-efficient multi-crystalline silicon solar cells with novel nanoscale pseudo-pyramid texture, Adv. Funct. Mater. 24 (2014) 6708–6716.

[15] G. Xiao, B. Liu, J. Liu, Z. Xu, The study of defect removal etching of black silicon for solar cells, Mater. Sci. Semicond. Process. 22 (2014) 64–68.

[16] S. Liu, X. Niu, W. Shan, W. Lu, J. Zheng, Y. Li, H. Duan, W. Quan, W. Han, C.R. Wronski, D. Yang, Improvement of conversion efficiency of multicrystal-line silicon solar cells by incorporating reactive ion etching texturing, Sol. Energy Mater. Sol. Cells 127 (2014) 21–26.

[17] J. Yoo, G. Yu, J. Yi, Large-area multicrystalline silicon solar cell fabrication using reactive ion etching (RIE), Sol. Energy Mater. Sol. Cells 95 (2011) 2–6.

[18] M. Schnell, R. Lüdemann, S. Schaefer, Plasma surface texturization for multi-crystalline silicon solar cells, in: Proceedings of the 28th IEEE Photovoltaics Specialists Conference, IEEE Electron Devices Society, Anchorage, Alaska, USA, 2000, pp. 367–370.

[19] J. Zhao, M.A. Green, Optimized antireflection coatings for high-efficiency silicon solar cells, IEEE Trans. Electron Devices 48 (1991) 1925–1934.

[20] V. Shanmugam, J. Cunnusamy, A. Khanna, P.K. Basu, Z. Yi, C. Chilong, A.F. Stassen, M.B. Boreland, T. Mueller, B. Hoex, A.G. Aberle, Electrical and microstructural analysis of contact formation on lightly doped phosphorus emitters using thick-film Ag screen printing pastes, IEEE J. Photovolt. 4 (2014) 168–174.

[21] M.Z. Burrows, A. Meisel, D. Balakrishnan, A. Tran, D. Inns, E. Kim, A.F. Carroll, K.R. Mikeska, Front-side Ag contacts enabling superior recombination and fine-line performance, in: Proceedings of the 39th IEEE Photovoltaic Specialists Conference (PVSC), 2013, pp. 2171–2175.

[22] M. Spitz, U. Belledin, S. Rein, Fast inductive inline measurement of the emitter sheet resistance in industrial solar cell fabrication, in: Proceedings of the 22nd European Photovoltaic Solar Energy Conference, Milan, 2007, pp. 47–50.

[23] J. Krupka, Contactless methods of conductivity and sheet resistance measurements for semiconductors, conductors and superconductors, Meas. Sci. Technol. 24 (2013) 13.

[24] Synopsys, Sentaurus™ User Guide, release I-2013.12 in, Zurich, Switzerland, 2013.

[25] J. Schön, A. Abdollahinia, R. Müller, J. Benick, M. Hermle, W. Warta, M.C. Schubert, Predictive simulation of doping processes for silicon solar cells, Energy Proced. 38 (2013) 312–320.

[26] P. Repo, J. Benick, Gv Gastrow, V. Vähänissi, F.D. Heinz, J. Schön, M.C. Schubert, H. Savin, Passivation of black silicon boron emitters with atomic layer deposited aluminum oxide, Phys. Status Solidi (RRL) – Rapid Res. Lett. 7 (2013) 950–954.

[27] W. Kern, D. Puotinen, Cleaning solutions based on hydrogen peroxide for use in silicon semiconductor technology, RCA Rev. 31 (1970) 187–205.

[28] B. Hoex, J.J.H. Gielis, M.C.M. van de Sanden, W.M.M. Kessels, On the c-Si surface passivation mechanism by the negative-charge-dielectric Al$_2$O$_3$, J. Appl. Phys. 104 (2008) 113703.

[29] G. Dingemans, N.M. Terlinden, M.A. Verheijen, M.C.M. van den Sanden, Controlling the fixed charge and passivation properties of Si(100)/Al$_2$O$_3$ interfaces using ultrathin SiO$_2$ interlayers synthesized by atomic layer deposition, J. Appl. Phys. 110 (2011) 1–6.

[30] P. Saint-Cast, D. Kania, M. Hofmann, J. Benick, J. Rentsch, R. Preu, Very low surface recombination velocity on p-type c-Si by high-rate plasma-deposited aluminum oxide, Appl. Phys. Lett. 95 (2009) 151502.

[31] A. Richter, J. Benick, A. Kimmerle, M. Hermle, S.W. Glunz, Passivation of phosphorus diffused silicon surfaces with Al$_2$O$_3$: Influence of surface doping concentration and thermal activation treatments, J. Appl. Phys. 116 (2014) 243501.

[32] G.K. Reeves, H.B. Harrison, Obtaining the specific contact resistance from transmission line model measurements, IEEE Electron Device Lett. 3 (1982) 111–113.

[33] D.K. Schroder, D.L. Meier, Solar cell contact resistance – a review, IEEE Trans. Electron Devices ED-31 (1984) 637–647.

[34] H.-C. Yuan, V.E. Yost, M.R. Page, P. Stradins, D.L. Meier, H.M. Branz, Efficient black silicon solar cell with a density-graded nanoporous surface: Optical properties, performance limitations, and design rules, Appl. Phys. Lett. 95 (2009) 123501.

[35] J. Hanoka, R. Bell, Electron-beam-induced currents in semiconductors, Annu. Rev. Mater. Sci. 11 (1981) 353–380.

[36] S. Kluska, C. Fleischmann, A. Büchler, W. Hördt, C. Geisler, S. Hopman, M. Glatthaar, Micro characterization of laser structured solar cells with plated Ni–Ag contacts, Sol. Energy Mater. Sol. Cells 120 (2014) 323–331.

[37] C. Donolato, The relation between EBIC contrast and recombination velocity of a grain boundary, Mater. Sci. Eng. B 24 (1994) 61–63.

[38] Z. Shen, B. Liu, Y. Xia, J. Liu, J. Liu, S. Zhong, C. Li, Black silicon on emitter diminishes the lateral electric field and enhances the blue response of a solar cell by optimizing depletion region uniformity, Scr. Mater. 68 (2013) 199–202.